# A neutral pH aqueous biphasic system applied to both static and flow membrane-free battery

Paula Navalpotro [*], Santiago E. Ibañez, Eduardo Pedraza, Rebeca Marcilla [*]

*Electrochemical Processes Unit, IMDEA Energy Institute, Avda. Ramón de La Sagra 3, Móstoles 28935, Spain*

ABSTRACT

Here, we present a new aqueous biphasic system (ABS) with near neutral pH and containing highly soluble organic/organometallic active species that avoids crossover due to the thermodynamic separation of active species. This ABS become the best example of "*Static*" Membrane-Free Battery with the highest maximum theoretical energy density (21.7 Wh L$^{-1}$), enhanced coulombic efficiency (96%) and stable performance over 250 cycles. Moreover, this work assesses the process of the self-discharge stablishing for the first time a protocol to quantify this phenomenon that results in low coulombic efficiencies in membrane-free batteries. Remarkably, a radically new membrane-free flow-reactor was specifically designed to maintain a stable liquid-liquid interphase that allows the battery to operate under flowing conditions. This resulted in flow battery with a two-fold increase of power density, high coulombic efficiencies and excellent capacity retention over 100 cycles. This work demonstrates for the first time the feasibility of this biphasic electrolyte concept in a truly Membrane-free "*Flow*" Battery.

## 1. Introduction

The growing energy demand is boosting the deployment of renewable energies [1]. However, their inherent intermittence makes essential their storage to meet the demand and the production. Redox flow batteries (RFBs) stand out due to their efficiency, flexibility, modularity, and their unique feature of decoupling power and energy density [1]. The most widely deployed example of this technology is the all-vanadium RFB (VRFB), where both catholyte and anolyte are aqueous acidic solutions of vanadium species separated by a Nafion membrane [2,3]. The role of the membrane is to avoid the short-circuit and the cross-mixing of electrolytes while allowing ion carriers going through [4]. The scarcity and fluctuating price of vanadium, the high price of ion-exchange membranes, and the limited operational temperature range of catholyte limit the wide implementation of VRFBs [5,6]. In the last few years, a growing scientific interest has been renovated to develop more sustainable and cost-efficient RFBs becoming a flourishing field of research [7–10].

For example, the replacement of ion-selective membranes by less expensive porous separators have been possible by using mixed electrolytes [11], symmetric electrolytes [12] redox-active polymers [13] or semisolid electrolytes [14]. However, they have important

disadvantages as high electrolyte viscosity, flowable difficulties and/or low active species concentration. Another promising research topic is the development of aqueous organic redox flow batteries (AORFB) in which vanadium species are replaced by organic redox molecules made of abundant elements [10,15,16]. Besides evident benefits in terms of sustainability and cost, organic chemistry offers multiple possibilities to functionalize a molecular structure tuning important properties such as solubility, stability or redox potential. Although numerous organic and organometallic species have been reported as active species in AORFB significant capacity fading and limited life-time are commonly observed due to degradation of the active species (mutual incompatibility, descomposition…) and inevitable cross-contamination through the membrane [17–19]. This crossover does not lead to permanent capacity fade in VRFB since it can be recovered via electrolyte rebalancing. Unfortunately, in AORFB the cross-over results in irreversible capacity loss due to chemical instability and parasitic reactions between organic active species [20–22].

In 2017, Navalpotro *et al.* proposed a new membrane-free battery approach which relies on the use of immiscible electrolytes and employs soluble organic redox species [23]. Different from conventional RFB where crossover is determined by the effectiveness of the ion-selective membrane, here the cross-over was only dictated by thermodynamics.

* Corresponding authors.
*E-mail addresses:* paula.navalpotro@imdea.org (P. Navalpotro), rebeca.marcilla@imdea.org (R. Marcilla).

First examples were devoted to aqueous-nonaqueous immiscible systems containing different type of active species (*eg.*, quinones, viologens, TEMPOs, metallic salts, etc.) [24–27,28,29]. This combination of aqueous-non aqueous electrolytes was also used in the so called membrane-free hybrid batteries in which one of the active species is Zn foil used as anode [30,31]. Although some aspects such as self-discharge can be mitigated, the main drawback of this hybrid technology is that energy and power are not decoupled as in conventional RFB. Other problems derived from the use of Zn anode such us the corrosion and dendritic growth also limits its lifetime.

Later, the concept of membrane-free battery was expanded to two aqueous-aqueous immiscible redox electrolytes becoming into more sustainable, environmentally friendly and less expensive battery chemistry [32]. Recently, Navalpotro et al. reported the first totally aqueous Membrane-Free Battery using an Aqueous Biphasic System (ABS) containing methyl viologen and TEMPO as anolyte and catholyte redox species, respectively [33]. The membrane-free battery showed an open circuit voltage (OCV) of 1.23 V, adequate partition coefficients of active species and excellent long-cycling performance at low state of charge (5% SOC). However, it also showed important drawbacks like restrained coulombic efficiency (CE≤68%) due to self-discharge and low theoretical capacity (2.68 Ah L$^{-1}$) and energy density (1.6 Wh L$^{-1}$) owing to the low solubility of TEMPO (~0.1 M) [33].

Here, we overcome the abovementioned limitations and proposed a new membrane-free battery based on an ABS formed by PEG$_{1000}$ and (NH$_4$)$_2$SO$_4$ containing methyl viologen dichloride (MV) and (ferrocenylmethyl)trimethylammonium chloride (FcNCl) in the anolyte and catholyte phases, respectively. Notably, the versatile and tunable composition of Aqueous Biphasic Systems (ABS) provides a precise control of the pH, solubility, redox reversibility and partition coefficients of the active species, being key aspects in the performance of the batteries. In this new ABS, having pH close to neutral, the active species present both adequate distribution in the two immiscible phases and high solubility (~1.5 M of MV in the anolyte and ~1.7 M of FcNCl in the catholyte) enabling high maximum theoretical energy density

(22.76 Wh L$^{-1}$), high coulombic efficiency (96%), and long-term stability (>250 cycles) when applied in a membrane-free "*static*" battery. Equally important, by using a home-design flow-through reactor, the proposed membrane-free battery was operated under flow conditions reaching higher power density. The battery exhibited a stable and efficient performance constituting the first example of Membrane-Free Redox Flow Battery.

## 2. Results and discussion

In the previously reported membrane-free battery, the ABS was formed by PEG and Na$_2$SO$_4$ and the performance was limited by the catholyte capacity due to the low solubility of TEMPO in the top phase [33]. Here, we propose to substitute TEMPO by highly soluble FcNCl but the moderate electrochemical performance of FcNCl in Na$_2$SO$_4$ supporting electrolyte (Figs. S1-SI) encouraged us to develop alternative ABS. Hence, we explored the use of (NH$_4$)$_2$SO$_4$ as solute in a new ABS since it enables the most stable electrochemistry of FcNCl (Figs. S1-SI).

The binodal curve of the ABS composed by PEG$_{1000}$, (NH$_4$)$_2$SO$_4$ and water was determined by cloud-point titration and it is represented in Fig. 1a. The composition and the mass of the top (TP) and bottom phases (BP) is given by the thermodynamic equilibrium represented by the intersection of the tie-line with the binodal curve and by the length of the two segments of the tie line, respectively (Table S1-S2-SI). Therefore, a mixture point composed by 25 wt% PEG$_{1000}$, 18 wt% (NH$_4$)$_2$SO$_4$ and 57 wt% water was selected to obtain similar volume of immiscible electrolytes for the Membrane-free battery (Fig. 1b). The composition and other properties of the top phase (TP) and the bottom phase (BP) were determined and included in Table 1. The two phases showed similar density and pH but very different values of conductivity which is attributed to the different composition. Indeed, the salt-rich BP presents much higher ionic conductivity likely due to the higher content of salt (2.82 M vs. 0.123 M for TP). This different composition influences directly on the active species partitioning behavior of the future battery.

In order to become a battery, MV and FcNCl were added as highly
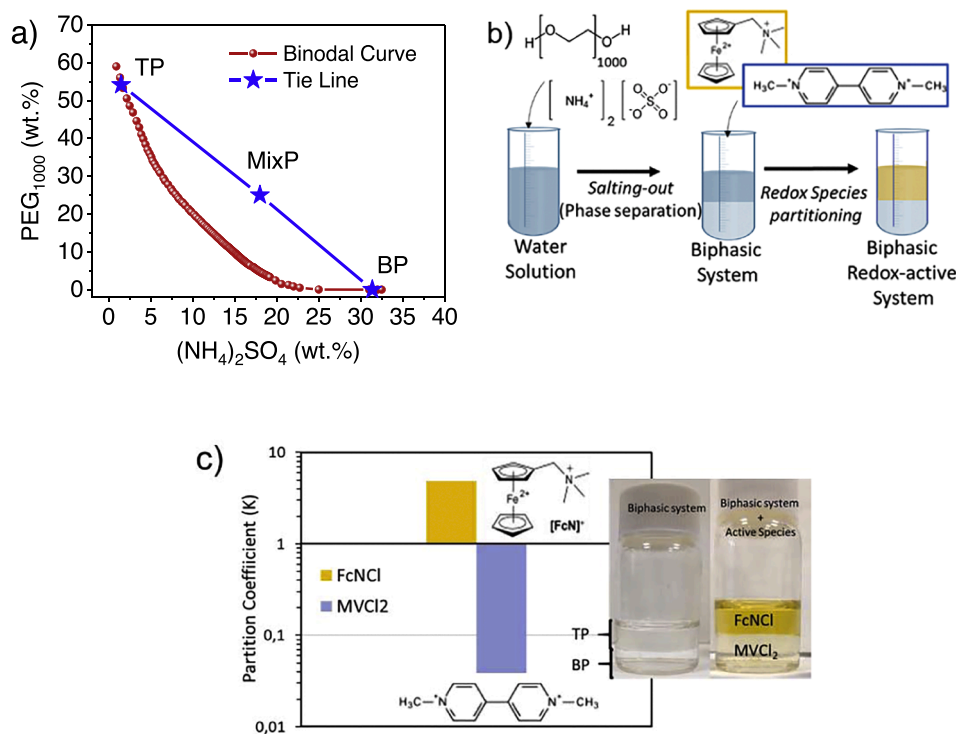


**Fig. 1.** a) Phase diagram and tie line of the biphasic system formed by PEG$_{1000}$ + (NH$_4$)$_2$SO$_4$. b) schematic representation of the phase separation process from the selected mixture point. c) partition coefficient of active species determined by UV–vis (inset: photo of biphasic system without and with dissolved active species).

**Table 1**

Composition and physic-chemical properties of each phase of the biphasic system formed by $PEG_{1000} + (NH_4)_2SO_4$ at a certain mixture point (MixP).

|  | $PEG_{1000}$ (% wt) | $(NH_4)_2SO_4$ (% wt) | $H_2O$ (% wt) | $PEG_{1000}$ (M) | $(NH_4)_2SO_4$ (M) | Density (g mL$^{-1}$) | Conductivity (mS cm$^{-1}$) | pH |
|---|---|---|---|---|---|---|---|---|
| MixP | 25 | 18 | 57 | – | – | – | – | – |
| TP | 54.14 | 1.4853 | 44.37 | 0.596 | 0.123 | 1.1016 | 2.78 | 5.4 |
| BP | 0.0185 | 31.37 | 68.61 | $2.19 \cdot 10^{-4}$ | 2.82 | 1.1866 | 225 | 5.3 |

soluble active species to the ABS (see Fig. 1b). This chemistry has been already employed as anolyte and catholyte, respectively, in conventional ORFB [34–41]. However, as most of the organic active species, MV and FcNCl are electrochemically incompatible (Figs. S2 and S3-SI), which obliges to keep them separated avoiding any cross-contamination and its consequently irreversible degradation. In conventional RFB, the effectiveness of separation depends on the quality of the ion-selective membrane, whereas in this membrane-free battery concept, the species are separated by thermodynamics through the partitioning co-efficients, which might be more effective than any membrane. When added to the ABS, the FcNCl has high affinity for the TP (yellow colored phase in Fig. 1c inset), whereas MV is selectively dissolved in the BP, thus TP will act as catholyte and BP as anolyte in the battery. Indeed, the partition coefficients (K) measured by UV (Figs. S4-SI, Fig. 1c) are 4.88 and 0.039 for FcNCl and MV, respectively. This means that MV is practically confined to the BP (with 25 times higher concentration in the BP than in the TP) whereas FcNCl is almost 5 times more concentrated in the TP than in the BP. This partitioning behavior is attributed to the hydrophilic character of MV which tends to be dissolved in the hydrophilic phase (BP) whereas FcNCl that is more hydrophobic tends to be dissolved in the TP (PEG-rich). Interestingly, the compatibility study shows that the electrochemistry of FcNCl is drastically affected by the presence of MV whereas MV is electrochemically stable with FcNCl (Figs. S2-SI). Therefore, the obtained partition coefficients meet with the compatibility requirements for both compartments, being more exigent in the case of MV that is practically absent in the catholyte ($K_{MV}=0.039$).

After adding the active species, each phase was electrochemically investigated. Cyclic voltammetries (CVs) in Fig. 2a show the redox peaks attributed to well-stablished reaction mechanisms for MV in the BP (anolyte) and for FcNCl in the TP (catholyte) (see Fig. 2b). The redox potentials of FcNCl ($E_{1/2catholyte}$) and MV ($E_{1/2anolyte}$) were 0.35 V and −0.74 V, respectively, anticipating an OCV of 1.1 V which is similar or even higher than for conventional RFB using same species [34,35,37]. The adequate selective partitioning of active species in the ABS was confirmed by CV (Figs. S5-SI), where just small signal of FcNCl was detected in the anolyte (BP) and almost no signal from MV was observed in the catholyte (TP). Moreover, the kinetics and diffusion parameters of each electrolyte were determined by detailed CV analysis (Figs. S6-SI) and listed in Table 2. The diffusion coefficients (D) were found to be $3.39 \cdot 10^{-6}$ and $4.89 \cdot 10^{-7}$ cm$^2$ s$^{-1}$ for MV in the anolyte and FcNCl in the

**Table 2**

Electrochemical, kinetic and diffusion parameters calculated for the electrolytes.

|  | $E_{1/2}$ (V vs Ag/Ag/Cl) | $\Delta E_p$ (mV) | $k^0$ (cm s$^{-1}$) | D (cm$^2$ s$^{-1}$) |
|---|---|---|---|---|
| FcNCl in TP-Catholyte | 0.35 | 207 | $5.46 \cdot 10^{-5}$ | $4.89 \cdot 10^{-7}$ |
| MV in BP- Anolyte | −0.74 | 59 | $> 10^{-1}$ | $3.39 0 \cdot 10^{-6}$ |

catholyte, respectively. The D for MV is similar of those reported in conventional aqueous electrolytes [34,35,39,40] whereas the D of FcNCl is significantly lower. This is probably due to the high concentration of $PEG_{1000}$ in the catholyte that indeed increases the viscosity and reduces the species mobility. The high rate constant values ($k^0$) of FcNCl and MV ($5.46 \cdot 10^{-5}$ cm s$^{-1}$ and a $k^0 > 10^{-1}$ cm s$^{-1}$, respectively) are similar or even higher than those obtained in conventional supporting electrolytes and imply fast kinetics [35,41]. Additionally, the CVs of the bottom and top phases of our biphasic system (Figs. S7-SI) showed that CV of MV is invariant during 100 cycles (although a small amount of FcNCl, determined by the partition coefficient, is present). Moreover, the CV of the FcNCl in the top phase shows small variations over the cycles but not significant changes despite of the presence of a small amount of MV. Note that CV of mixed electrolytes (containing same concentration of MV and FcNCl) (Figs. S2b-SI) showed high degradation rate of FcNCl after 100 cycles. These results confirm the viability of this ABS as stable redox immiscible electrolytes since the partition coefficients of MV and FcNCl are high enough to selectively keep the active species separated avoiding parasitic reactions.

Considering the promising electrochemical behavior of individual electrolytes, a "*static*" membrane-free battery was assembled introducing two carbon felt electrodes in the redox-active ABS. Notice that no separator was used in the experimental set-up (Fig. 3a). Fig. 3b shows stable potential plateaus for the cell and for individual electrolytes when the battery is galvanostatic charged/discharged at C/4 (see experimental section for C-rate and current values details). Battery voltage and individual potentials are very close to the ones anticipated by CV demonstrating low overpotentials for redox reactions. Remarkably, the voltage difference at the interface keeps constant at low potential (∼ 95 mV) which confirms the low resistance at the liquid-liquid interface.
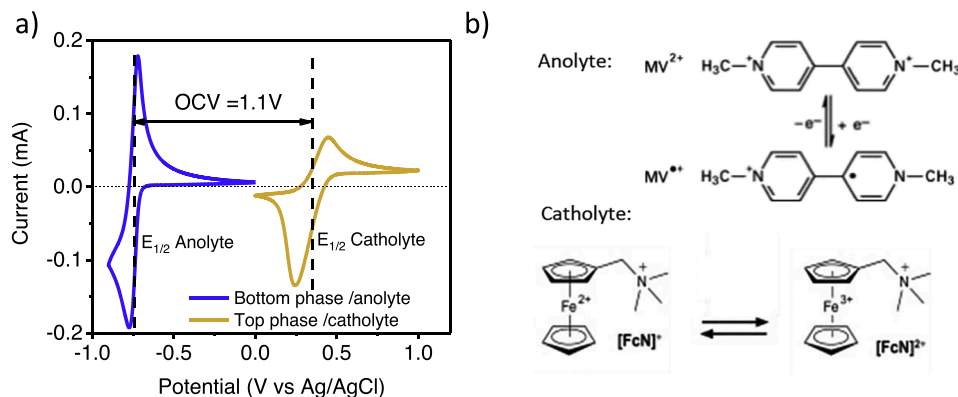


**Fig. 2.** a) cyclic voltammetry of each phase of the system with 20 mM active species concentration at 10 mV s$^{-1}$. b) Scheme of redox reaction of MV in the anolyte and FcNCl in the catholyte.
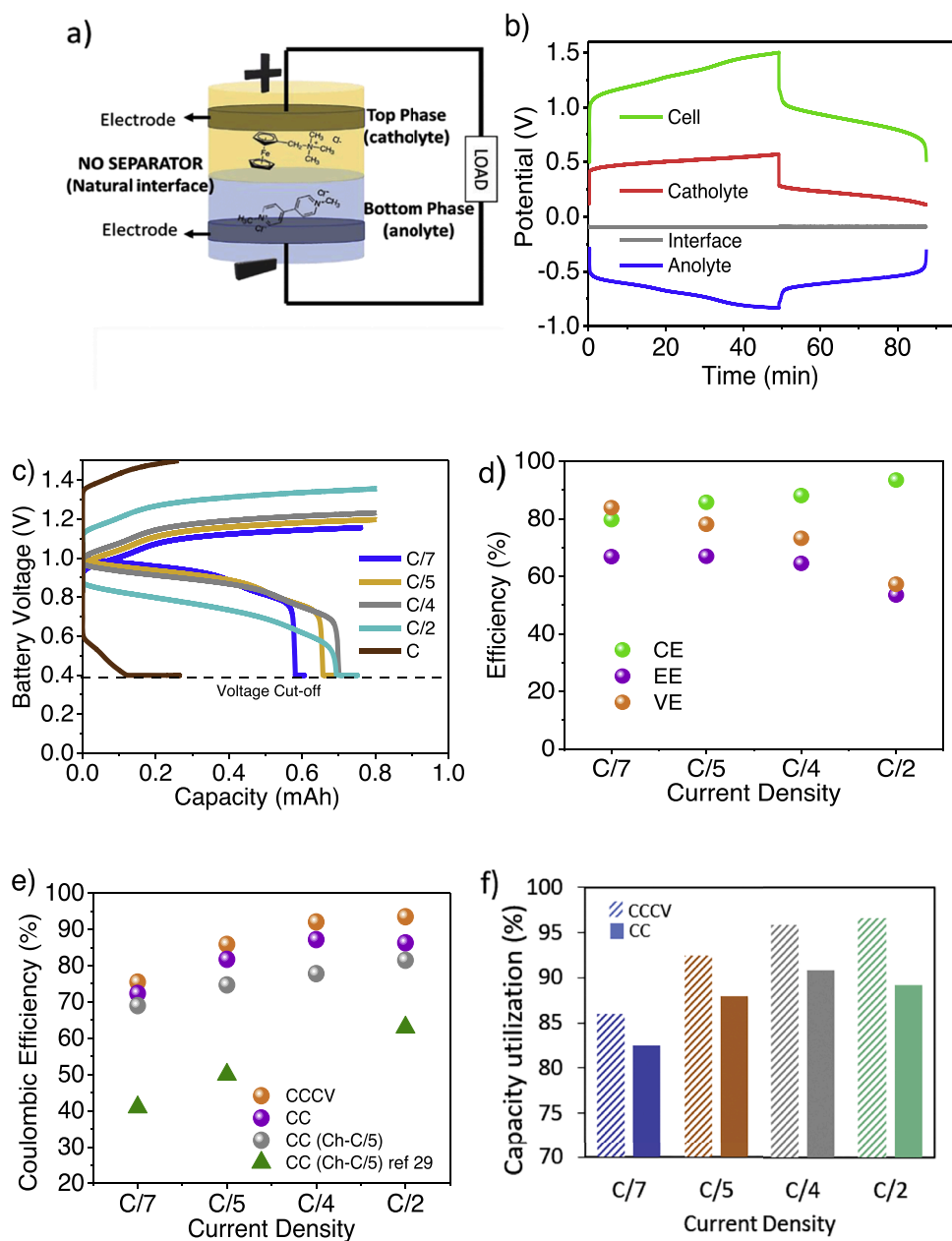
**Fig. 3.** a) Schematic representation of membrane-free "static" battery. b) Galvanostatic charge-discharge of low concentrated "static" battery (20 mM active species concentration) at C/4 and 20% SOC; c) CC charge and CCCV discharge profile of "static" battery (0.1 M) at different C-rate (20% SOC); d) Efficiency analysis at different C-rate (CCCV discharge): Coulombic efficiency (CE), Voltage efficiency (VE) and Energy Efficiency (EE). e) Dependence of coulombic efficiency with characterization conditions: Same current for charging and discharging with galvanostatic +potenciostatic step (CCCV) (in orange); Same current for charging and discharging only galvanostatic step (CC) (in purple); CC density for charge (C/5) and different current for discharging only galvanostatic step (CC Ch-C/5) (in gray); data in green triangle were obtained in similar experimental conditions[29]: CC density for charge (C/5) and different current for discharging only galvanostatic step (CC Ch-C/5). f) Capacity utilization at different C-rates comparing only CC (solid color) and CCCV discharge conditions (striped color).

This is a significant advantage of this membrane-free concept compared with the high contribution of the membrane (70–90%) to the battery resistance in conventional designs [35,39]. However, coulombic efficiency of the cycle is only 78% due to the self-discharge of the membrane-free battery. This phenomena is an inherent aspect to membrane-free batteries and consists on the recombination of charged species at the interphase resulting in low coulombic efficiencies (CE) and low capacity utilization values (Fig. S11a) [33]. The self-discharge is a complex process that depends on several factors including recombination reaction kinetics, diffusion of active species, concentration of charged species (~SOC), electrolyte residence time, etc.

In order to get deeper insights into the effect of self-discharge in the performance of membrane-free batteries, we assembled a battery with higher active species concentration (0.1 M). The battery was galvanostatically charged-discharged at different C-rates with a final potentiostatic period holding the voltage at 0.4 V in discharge. These experimental conditions allowed us to maximize the discharge capacity eliminating the mass transport issues and ensuring the conversion of all the available active species. Fig. 3c shows a plateau for the discharge profiles at about 1 V with low overpotentials at low C-rates (from C/7 to C/4). At higher C-rates (C/2) the ohmic resistance becomes significant (~160 mV) but still shows a quite stable voltage plateau. However, at 1C the large overpotential limits both the charge and the discharge. Fig. 3d shows that the voltage efficiency (VE) decreases with the current density due to the larger overpotentials at higher currents. On the contrary, the low coulombic efficiency at C/7 (CE~ 80%) which is attributed to the self-discharge at the interphase, increases at higher C-rates reaching a maximum as high as 93.5% at C/2 (Fig. 3d). This increasing trend might be attributed to the lower self-discharge in the shorter cycles (Figs. S8-SI) considering that this self-discharge is a time-dependent process, thus the shorter the cycles the lesser the self-discharge. Indeed, different charging protocols also leads to different CE with the lower efficiency in those charged at constant C/5 and discharged at different C-rates (see Fig. S9 and compare gray vs. purple dots in Fig. 3e). Note that small differences (3–5%) in the reported CE between gray and purple dots at C/7 and C/5 are attributed to experimental errors, since both

experiments were performed in similar batteries but not in the same one. Interestingly, the battery reported here and based on ABS containing MV and FcN active species, showed remarkable improvement of CE compared to previous example of membrane-free battery (green vs. gray in Fig. 3e) [33].

Since the self-discharge is a general drawback of the membrane-free battery concept, that limits the SOC and the CE, this work assesses the process of the self-discharge elucidating and stablishing for the first time a protocol to quantify this phenomenon. Indeed, a better understanding on the self-discharge phenomenon and its basis will contribute to design strategies to mitigate this limitation while increasing attainable SOC. A detailed analysis of the capacity utilization considering the capacity losses attributed to self-discharge and to diffusion limitation issues was performed (see Materials and methods section for further details). Fig. 3f shows that the capacity utilization increased with increasing current density reaching up to 96.6% at C/2 when potentiostatic step is considered (under galvanostatic conditions maximum capacity utilization of 90.6% was obtained at C/4). Not surprisingly, in all the cases capacity utilization is higher if an additional potentiostatic stage is performed. This difference confirms that under galvanostatic conditions, diffusion limitations cause a Remnant Capacity ($C_R$) and consequently lower Capacity utilization. The contribution of the diffusion limitation ($C_R$) and the self-discharge ($C_{SD}$) to the total capacity utilization were estimated for the first time in this membrane-free battery concept and represented in Fig. S10 (see materials and methods section for further details). This analysis shows that although battery self-discharge is high at low C-rates ($C_{SD}$ of 24% at C/7) this phenomenon was minimized at moderate rates where losses due to diffusion limitation are still modest ($C_{SD}$ and $C_R$ ~7% at C/2). In addition to this analysis, another self-discharge experiment was performed consisting on the recording of the OCV of the charged battery (20%SOC) over time (Fig. S11b). From the lineal part of the OCV curve in this experiment, it can be extracted that the voltage decay over time is around 12 mV·h$^{-1}$ evidencing a moderate self-discharge rate in static conditions. In fact, the time at which the voltage drops is evident (8 h) yields a length of the diffusion

layer ($l \sim \sqrt{D \cdot t}$) of ~12 mm which is of the order of magnitude of the height of each electrolyte compartment. It is therefore the time it takes for all existing active species present in the battery to encounter opposing charged species.

Additionally, an extended galvanostatic charge-discharge study at C/5 displayed a high stable battery performance over 200 cycles (~16.5 days) (Figs. 4a-b), showing stable values of coulombic efficiency (85–88%) with excellent capacity retention. In order to minimize the self-discharge while maximizing the discharge capacity, cyclability test at higher C-rate (C/2) and incorporating a potentiostatic step was also performed (Fig. 4c). Fig. 4d shows, after just 3 cycles of conditioning, that coulombic efficiency was maintained as high as 96% with 100% capacity retention over more than 250 cycles. It is important to remain that a conventional filter press redox flow battery employing MV and FcNCl mixed electrolytes totally lost its capacity in less than 50 cycles with a remarkable capacity decay after only 10 first cycles (Figs. S3-SI). Note that this is the first time that an experimental evidence about their mutual incompatibility of MV and FcNCl is provided. CV curves of fresh and cycled electrolytes are very similar with same peak intensities demonstrating that no significant crossover occurs during the battery operation (Figs. S12-SI). This evidences that the thermodynamic separation of incompatible active species in the biphasic electrolytes was efficient over cycling avoiding parasitic reactions, being an advantage of this type of membrane-free battery. These high coulombic efficiencies and long-term stability are particularly relevant compared to the modest data published so far for membrane-free battery at significant state of charge [23,33]. A complete comparison with conventional viologen/ferrocene RFB and with state-of-the-art aqueous membrane-free batteries was included in Tables S3-S4-SI.

The promising performance of this "*static*" battery encourage us to test this battery chemistry under flowing conditions becoming the first example of membrane-free "*flow*" battery with aqueous immiscible electrolytes. Due to interphase instabilities and other issues, membrane-free battery technology was doomed to remains as a "*static*" technology so far. However, a new "homemade" patented [42] reactor specifically
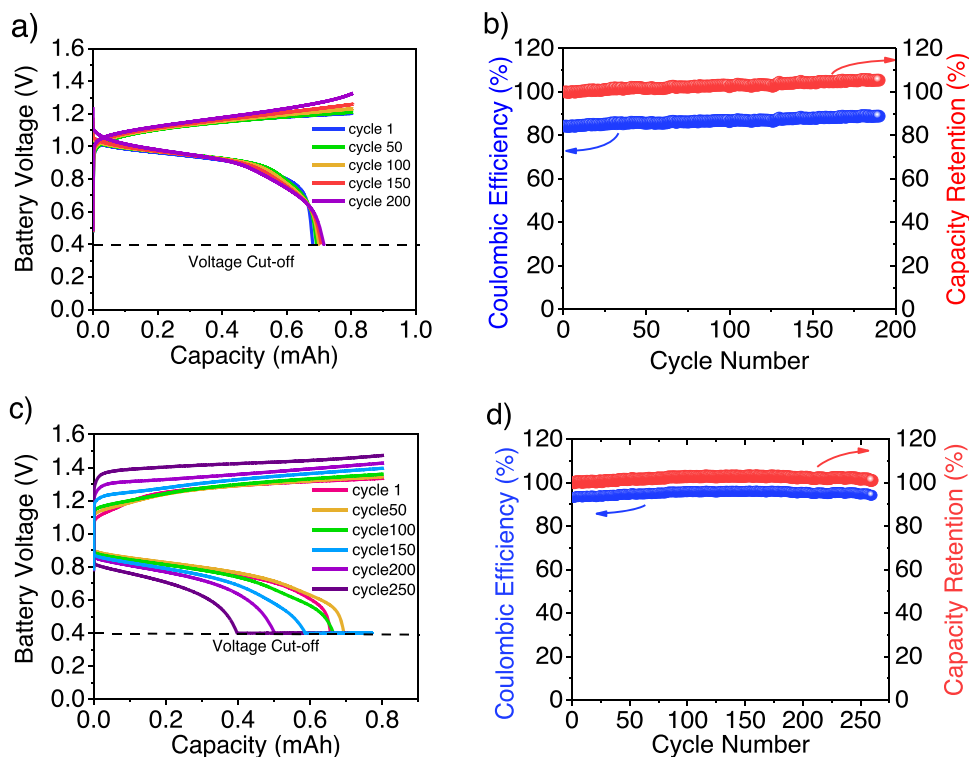


**Fig. 4.** Cycling performance of membrane-free "static" battery. Active Species Concentration 0.1 M. Battery SOC 20%. a) galvanostatic charge/discharge profile at C/5. b) CE and capacity retention at C/5. c) galvanostatic+ potenciostatic discharge profile at C/2. d) CE and capacity retention at C/2.

designed to operate with any combination of immiscible electrolytes to develop membrane-free redox flow batteries was used in this work (Fig. 5a). Operating the battery under flowing conditions will cause that the "charged" electrolyte is rapidly pumped out of the reactor reducing the residence time of the charged species inside the reactor. In such reactor, immiscible electrolytes are pumped into the horizontal cell in perpendicular direction to the liquid-liquid interface which favors the formation of a stable interphase under flowing regime. This discovery restores the capacity to decouple energy and power in membrane-free batteries, being a key aspect in battery technology. The membrane-free "*flow*" battery was first subjected to polarization test at different flow rates (Fig. 5b). At low flow rate (6 mL min$^{-1}$) mass transport limitation occurs at currents > 7 mA cm$^{-2}$ whereas this transport constraint is mitigated increasing the flow rate up to 13.5 mL min$^{-1}$. Tested flow rates (up to 44 mL min$^{-1}$) correspond to stable conditions for the liquid-liquid interface at any time with no visible deformation. Remarkably, in comparison with the membrane-free "*static*" battery, the "*flow*" battery achieved much higher currents and a two-fold peak power density. This improvement is attributed to the lesser transport limitation at the electrode surface when the electrolyte is forced to flow-through the electrode [42]. In order to confirm that the liquid-liquid interphase is stable and turbulences does not hinder the performance, the *flow* battery was subjected to long-term charge-discharge experiment during 100 cycles. Similarly to the static one, after 5 cycles of conditioning, Fig. 5c-d shows stable performance with clear voltage plateaus keeping a high CE (90–94%) and excellent capacity retention (100%).

## 3. Conclusions

In summary, this work shows a totally aqueous membrane-free battery based on immiscible electrolytes that can be operated either in *static* or *flow* conditions. The composition of the new aqueous biphasic electrolytes, containing highly soluble methylviologen/ferrocene derivative active species, results in a battery with high maximum theoretical energy density (21.7 Wh L$^{-1}$). Moreover, the adequate partition coefficients of active species allow efficient separation and avoids cross-contamination during long cycling. Thus, the *static* battery shows high CE (96%), high capacity utilization (96.6%) and long-time stability along 250 cycles without capacity fading. In addition, experiments under static conditions provide significant insights about the self-discharge process and tools to minimize it. By using a new homemade patented flow-reactor, the battery becomes the first example of aqueous membrane-free *flow* battery showing a stable performance exhibiting high CE (90–94%) and no capacity losses over 100 cycles. Although further optimization of the design and a deep analysis of critical aspects are still necessary, this work demonstrates, for the first time, the feasibility of a membrane-free "*flow*" battery based on aqueous immiscible electrolytes.

## 4. Materials and methods

### 4.1. Materials

Poly(ethylene glycol) MW 1000 (PEG$_{1000}$), ammonium sulfate (NH$_4$)$_2$SO$_4$, sodium sulfate anhydrous (Na$_2$SO$_4$, >99%), sodium chloride (NaCl), ammonium chloride (NH$_4$Cl), Methyl Viologen dichloride hydrate (MV, 98%), were purchased from Sigma Aldrich-Merck and used as received. (ferrocenylmethyl)trimethylammonium chloride (FcNCl) was synthesized as reported elsewhere [34].

### 4.2. Phase diagram determination

The phase diagram of the biphasic system formed by PEG$_{1000}$, (NH$_4$)$_2$SO$_4$ and water was determined by cloud-point titration method at room temperature (298 $K \pm 1$). The procedure is based on the dropwise addition of salt-aqueous solution into the polymer aqueous solution until a cloudy solution is detected. To return to a clear solution, water is drop-added. The salt-aqueous solution and polymer aqueous solution were prepared in advanced at 25 % wt and 60 % wt concentration, respectively. The procedure was carried out under continuous stirring. The experimental data for the phase diagram were determined
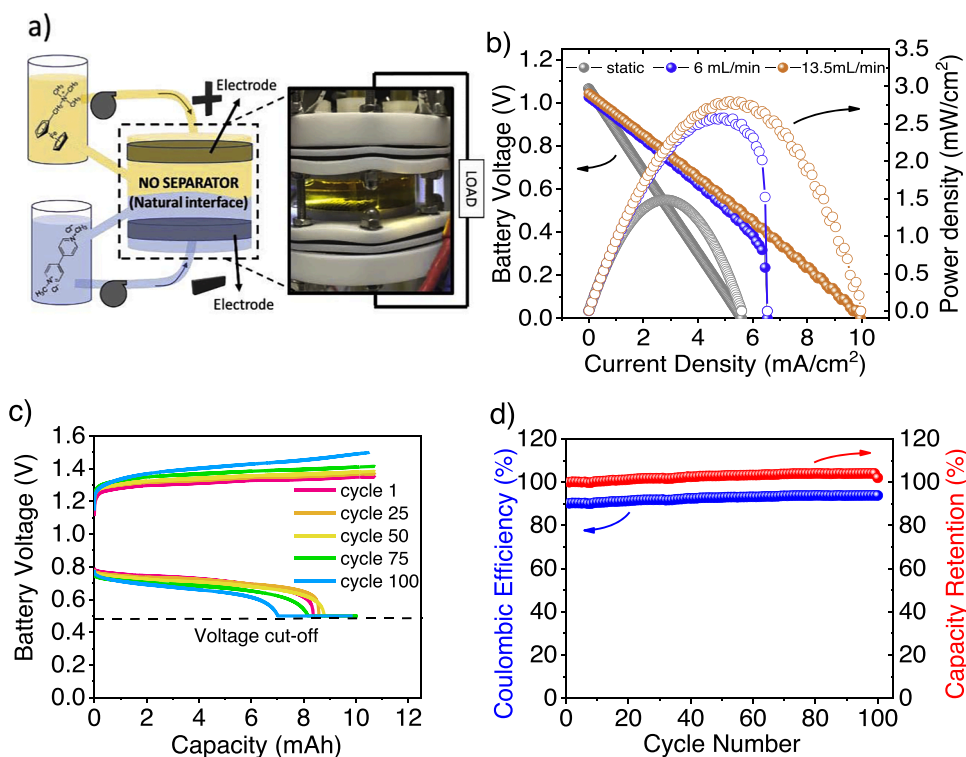


**Fig. 5.** Membrane-free "flow" battery performance. Active Species Concentration 0.1 M. a) Schematic representation of Membrane-free "flow" battery including a photo of the patented flow-reactor where the interphase formed by the two immiscible electrolytes is shown. b) Discharge polarization curves at different flow rates (and static conditions) at 20% SOC. c) galvanostatic charge and galvanostatic+ potenciostatic discharge profiles over 100 cycles at 2.8 mA cm$^{-2}$, 20%SOC and 13.5 mL min$^{-1}$ flow rate. d) CE and capacity retention over cycling.

gravimetrically ($\pm 10^{-4}$ g).

### 4.3. Binodal curve data fitting and tie line determination

The experimental data of the binodal curve were fitted by using the following equation developed by Merchuck et al. [43].

$$[Polymer] = A\exp\left[\left(B \times [Salt]^{0.5}\right) - \left(C \times [Salt]^3\right)\right] \tag{1}$$

where [*Polymer*] and [*Salt*] are the $PEG_{1000}$ and the $(NH_4)_2SO_4$ mass fraction percentages, and the parameters A, B and C are fitted constants.

In order to determine the tie line (TL), a ternary system was gravimetrically prepared by mixing $PEG_{1000}$, $(NH_4)_2SO_4$ and water at 25, 18, 57 wt%, respectively. Once the biphasic system is established the two liquid phases were separated and weighted. For the calculation of the TL the following 4 equation system was solved [43]. To determine the compositions of the top and bottom phase the lever-arm rule was applied.

$$[Polymer]_T = A\exp\left[\left(B \times [Salt]_T^{0.5}\right) - \left(C \times [Salt]_T^3\right)\right] \tag{2}$$

$$[Polymer]_B = A\exp\left[\left(B \times [Salt]_B^{0.5}\right) - \left(C \times [Salt]_B^3\right)\right] \tag{3}$$

$$[Polymer]_T = \frac{[Polymer]_M}{\alpha} - \frac{1-\alpha}{\alpha} \times [Polymer]_B \tag{4}$$

$$[Salt]_T = \frac{[Salt]_M}{\alpha} - \frac{1-\alpha}{\alpha} \times [Salt]_B \tag{5}$$

where the subscripts *T, B, M* indicate top phase, bottom phase and the initial mixture, respectively. [*Polymer*] and [*Salt*] are $PEG_{1000}$ and $(NH_4)_2SO_4$ wt fraction. The parameter α is the ratio between the top phase mass and the total mixture mass.

### 4.4. Partition coefficient determination

For evaluating the partitioning behavior of the active species, an ABS was gravimetrically prepared containing just one active species. Once the phases were separated and left overnight for reaching equilibrium, they were analyzed by UV spectrometry (UV–VIS LAMBDA 1050) and Eq. (6) was applied to obtain the partition coefficient.

$$K = \frac{[active\ specie]_{Top\ Phase}}{[active\ specie]_{Bottom\ Phase}} \tag{6}$$

### 4.5. Solubility tests

Solubility of FcNCl, and MV was measured in the Top phase or ÇBotttom phase of the ABS by preparing dissolving the compound until reach a supersaturated solution in a 5.0 mL graduated flask.

### 4.6. Electrolyte preparation

The electrolytes/phases were formulated by gravimetrically preparing the ABS mixing $PEG_{1000}$, $(NH_4)_2SO_4$ and water at 25, 18, 57 wt%, respectively. Then, the corresponding amount of active species was added to reach the desired concentration in each phase considering the calculated partition coefficient of MV and FcNCl. Once the active species are dissolved in the ABS, it was kept for resting overnight before using them in electrochemical experiments.

### 4.7. Electrode material

Glassy carbon was used as working electrode for cyclic voltammetry experiments. For battery testing carbon felts (grade GFD 4.6 EA) (4.6 mm thickness) were purchased from SGL CARBON GmbH and used as

electrode material. In order to make them hydrophilic they were pretreated by applying 400°C for 4 h.

### 4.8. Assembly of "Static" and "Flow" membrane-free battery

The Membrane-free "*static*" battery was assembled just by putting the same volume (1.5 mL) of each electrolyte/phase in a glass cell with a carbon felt electrode (1.7 cm$^2$) immersed in each electrolyte/phase (either 20 mM or 0.1 M). The interphase area was 1.7 cm$^2$ and the distance between the electrodes was 0.7 cm. Two "static" batteries were assembled; one containing 20 mM and another with 0.1 M of active species. The electrolytes where in contact without any physical barrier between them. In the diluted static battery two Ag/AgCl reference electrodes were used to monitor the potential of the individual electrodes and the potential difference at the interphase. One reference electrode was introduced in each electrolyte and placed as close as possible to the liquid-liquid interphase.

For the assembly of membrane-free "flow" battery we employed a reactor patented by Montes et al. [42]. This battery reactor has a horizontal design that enables the possibility to precisely control the position of the liquid-liquid interphase inside the reactor. Its reaction chamber is delimited by a central glass cylinder and two taps made of polytetrafluoroethylene (PTFE) that harbor each of the carbon felt electrodes (9 cm$^2$ of area) placed at a distance of 1 cm. The two electrolytes are pumped through the carbon felt into the chamber where they are keep separated by a natural interphase (without any kind of separator between both liquids) before going out of the cell. The electrolytes are pumped into the cell through the electrodes in perpendicular direction to the interphase. In contrast to other "*flow-by*" reactors [42], this "*counter-flow*" design with the electrolytes entering the cell in perpendicular direction to the interphase allows to use high flow rates maintaining a constant position of the interphase. The reactor was piped using Tygon® tubing to a peristaltic pump (Masterflex® L/S Variable Speed) and to the external electrolyte tanks as in a conventional redox flow battery. The total volume of electrolyte was 20 mL per phase.

### 4.9. Electrochemical characterization of electrolytes

All the electrochemical experiments were performed at room temperature in a Biologic VMP multichannel potentiostat. Cyclic voltammetry (CV) experiments were carried out in a 3-electrode glass cell, using glassy carbon, platinum wire and Ag/AgCl (3.5 M KCl) electrode as working, counter and reference electrode, respectively. The characterization of electrolytes was carried out at different scan rates from 1 to 400 mV s$^{-1}$. Then, the representation of peak current versus square root of the scan rate was lineally fitted. The calculation of the diffusion coefficient (*D*) was performed by applying Eq. (7) for the anolyte (reversible process) and Eq. (8) for catholyte [44] (quasi-reversible process) to the obtained mathematical fitting equation.

$$slope = 2.69 \cdot 10^5 n^{3/2} ACD^{1/2} \tag{7}$$

$$slope = 2.99 \cdot 10^5 n^{3/2} \alpha^{1/2} ACD^{1/2} \tag{8}$$

where *A* is the area of the electrode, *n* is the number of exchanged electrons, *C* is the concentration of active species. The transfer coefficient (*α*) can be estimated from Eq. (9) where $E_p$ and $E_{p/2}$ correspond to the potentials at peak current and half the peak current, respectively.

$$\left|E_p - E_{\frac{p}{2}}\right| = \left(\frac{48}{\alpha n}\right) \tag{9}$$

The redox potential of each active species is centered between the anodic and cathodic peak potential:

$$E_{1/2} = \left(E_{pa} + E_{pc}\right)/2 \tag{10}$$

The open circuit voltage was calculated considering (11):

$$E_{cell} = E_{1/2catholyte} - E_{1/2anolyte} \tag{11}$$

The rate constant $k^0$ of the catholyte was calculated by applying Nicholson Eq. (12) [45].

$$k^0 = \psi \left[ \pi D \frac{nF\vartheta}{RT} \right]^{1/2} \tag{12}$$

where $\psi$ is a parameter dependent on the peak separation established by Nicholson [45], $F$ is Faraday constant, $\vartheta$ is the scan rate, $R$ is the ideal gasses constant, $T$ temperature (298.15 K) and the other parameters aforementioned. The peak separation is defined as $\Delta E_p = E_{pa} - E_{pc}$. The rate constant of the anolyte was assumed to be $k^0 > 10^{-1}$ cm s$^{-1}$ due to the high reversibility of the redox process ($\Delta E_p = 59$ mV).

### 4.10. Electrochemical characterization of membrane-free batteries

The membrane-free "*static*" batteries were galvanostatically charged-discharged from 0 to 20% state of charge (SOC) at different C-rates from C/7 to C with upper and lower voltage cut-off of 1.5 and 0.4 V, respectively. The C-rate was calculated considering the theoretical capacity of the battery at 20% SOC in all the experiments. Thus, a C-rate of 1C corresponds to a current density of 4 mA. The discharge polarization curve was obtained by current scan from 0 to 6 mA cm$^{-2}$. In some cases, in order to fully discharged the battery, a potentiontatic step at 0.4 V was carried out after the galvanostatic period. The duration of the potentiostatic step was controlled with a cut-off current criteria of $I < 0.05$ mA.

The membrane-free "*flow*" battery was cycled at 20% SOC, the experiment was based on galvanostatic charge at 2.8 mA cm$^{-2}$ with a voltage cut-off of 1.5 V and galvanostatic discharge at 2.8 mA· cm$^{-2}$ followed by a potenciostatic step at 0.5 V with 13.5 mL min$^{-1}$ as flow rate.

**Energy density calculation**. The theoretical energy density of the FcNCl/MV Membrane-free Battery was calculated using Eq. (13), where n is the number of electrons involved into the cell reaction, C is the lower concentration of two electrolytes, F is Faraday's constant, V is the cell voltage, and $\mu_v$ represents the factor of overall volumes of anolyte and catholyte ($\mu v = 1 +$ lower electrolyte concentration/ higher electrolyte concentration)

$$\text{energy density} (\text{Wh} / \text{L}) = nCFV/\mu_v \tag{13}$$

Maximum theoretical energy density is calculated considering the maximum solubility of the active species.

Generally, the coulombic efficiency (*CE*) of a battery is determined as the ratio between discharge capacity ($C_{DCH}$) and charge capacity ($C_{CH}$). Here, two slightly different equations are distinguished depending on the experimental discharge conditions; Eq. (14a) for only galvanostatic discharge (constant current, CC) and Eq. (14b) for galvanostatic plus potenciostatic discharge (constant current + constant voltage, CCCV). The voltage efficiency (*VE*) and energy efficiency (*EE*) of the battery were calculated considering the Eqs. (15) and (16).

$$CE_{CC}(\%) = \frac{C_{DCH, CC}}{C_{CH}} \cdot 100 \tag{14a}$$

$$CE_{CCCV}(\%) = \frac{C_{DCH, CCCV}}{C_{CH}} \cdot 100 \tag{14b}$$

$$VE\ (\%) = \frac{discharge\ voltage}{charge\ voltage} \cdot 100 \tag{15}$$

$$EE = CE \cdot VE \tag{16}$$

### 4.11. Analysis of the self-discharge

The capacity loss due to the self-discharge phenomena ($C_{SD}$) is expressed by Eq. (17) considering that any deviation from 100% of

coulombic efficiency is due to the self-discharge. This calculation was done assuming that no additional parasitic reactions take place. We consider this is a reasonable assumption based on the moderate working potentials of the battery and the high stability displayed by the electrolytes in the CV experiments in that potential range. Thus, in a complete charge-discharge cycle the capacity that is attributed to self-discharge ($C_{SD}$) was calculated as the difference between the charge capacity ($C_{CH}$) and the discharge capacity (measured under CCCV conditions, $C_{DCH\ CCCV}$), as represented by Eq. (17).

$$C_{SD} = C_{CH} - C_{DCH\ CC,CV} \tag{17}$$

This self-discharge that is due to the recombination of charged species at the interface occurs during both charge and discharge steps. The extend of the self-discharge will depend on the time the charged species are in contact. If charge/discharge steps are performed at the same current, the duration of both steps is the same and it might be assumed that similar loss of capacity due to self-discharge will occur in charge ($C_{SD}/2$) and in discharge ($C_{SD}/2$). Therefore, the available capacity at the end of the charge step ($C_{ACH}$) is calculated according to Eq. (18) as the charge capacity ($C_{CH}$) minus the capacity lost by self-discharge in that period ($C_{SD}/2$).

$$C_{ACH} = C_{CH} - (C_{SD} / 2) \tag{18}$$

### 4.12. Analysis of the capacity utilization

The capacity utilization (%) was calculated as the ratio between the discharge capacity ($C_{DCH}$) and the available capacity at the end of the charge step ($C_{ACH}$) as described in Eq. (19).

$$\text{Capacity utilization } (\%) = \frac{C_{DCH}}{C_{ACH}} \cdot 100 \tag{19}$$

In those experiments where the discharge current rate is very high, a fraction of the available capacity will not be discharged at the electrode during the galvanostatic step due to diffusion limitation issues. This term is named remnant capacity ($C_R$) and it is calculated according to either Eq. (20) considering that during the additional potentionstatic stage all the available charged species will react at the electrode. The effect of selfdischarge in the potentciostatic step was assumed to be negligible due to the low battery SOC at the beginning of the step

$$C_R = C_{DCH,\ CCCV} - C_{DCH,CC} \tag{20}$$

**Declaration of Competing Interest**

The authors declare there is no any competing interest.

## Supplementary materials

Supplementary material associated with this article can be found, in the online version, at doi:10.1016/j.ensm.2023.01.033.

## References

[1] P. Alotto, M. Guarnieri, F. Moro, Redox flow batteries for the storage of renewable energy: a review, Renew. Sustain. Energy Rev. 29 (2014) 325–335, https://doi.org/10.1016/j.rser.2013.08.001.

[2] K. Lourenssen, J. Williams, F. Ahmadpour, R. Clemmer, S. Tasnim, Vanadium redox flow batteries: a comprehensive review, J. Energy Storage 25 (2019) 100844, https://doi.org/10.1016/j.est.2019.100844.

[3] M. Skyllas-Kazacos, C. Menictas, The vanadium redox battery for emergency back-up applications, Proc. Power Energy Syst. Converging Mark. Melbourne, VIC, Australia (1997) 463–471, https://doi.org/10.1109/INTLEC.1997.645928.

[4] H. Zhang, X. Li, J. Zhang. Redox Flow Batteries: Fundamentals and Applications, 1st ed., CRC Press, November 2017, ISBN 9781498753944, pp. 444–pages.

[5] C. Zhang, T.S. Zhao, Q. Xu, L. An, G. Zhao, Effects of operating temperature on the performance of vanadium redox flow batteries, Appl. Energy 155 (2015) 349–353, https://doi.org/10.1016/j.apenergy.2015.06.002.

[6] K.E. Rodby, T.J. Carney, Y. Ashraf Gandomi, J.L. Barton, R.M. Darling, F.R. Brushett, Assessing the levelized cost of vanadium redox flow batteries with capacity fade and rebalancing, J. Power Sources 460 (2020), 227958, https://doi.org/10.1016/j.jpowsour.2020.227958.

[7] E. Sánchez-Díez, E. Ventosa, M. Guarnieri, A. Trovò, C. Flox, R. Marcilla, F. Soavi, P. Mazur, E. Aranzabe, R. Ferret, Redox flow batteries: status and perspective towards sustainable stationary energy storage, J. Power Sources 481 (2021) 228804, https://doi.org/10.1016/j.jpowsour.2020.228804.

[8] P. Leung, A.A. Shah, L. Sanz, C. Flox, J.R. Morante, Q. Xu, M.R. Mohamed, C. Ponce de León, F.C. Walsh, Recent developments in organic redox flow batteries: a critical review, J. Power Sources 360 (2017) 243–283, https://doi.org/10.1016/j.jpowsour.2017.05.057.

[9] J. Noack, N. Roznyatovskaya, T. Herr, P. Fischer, The chemistry of redox-flow batteries, Angew. Chem. Int. Ed. 54 (2015) 9776–9809, https://doi.org/10.1002/anie.201410823.

[10] X. Wei, W. Pan, W. Duan, A. Hollas, Z. Yang, B. Li, Z. Nie, J. Liu, D. Reed, W. Wang, V. Sprenkle, Materials and systems for organic redox flow batteries: status and challenges, ACS Energy Lett. 2 (2017) 2187–2204, https://doi.org/10.1021/acsenergylett.7b00650.

[11] J. Luo, B. Hu, C. Debruler, Y. Bi, Y. Zhao, B. Yuan, M. Hu, W. Wu, T.L. Liu, Unprecedented capacity and stability of ammonium ferrocyanide catholyte in pH neutral aqueous redox flow batteries, Joule 3 (2019) 149–163, https://doi.org/10.1016/j.joule.2018.10.010.

[12] T. Janoschka, C. Friebe, M.D. Hager, N. Martin, U.S. Schubert, An approach toward replacing vanadium: a single organic molecule for the anode and cathode of an aqueous redox-flow battery, ChemistryOpen 6 (2017) 216–220, https://doi.org/10.1002/open.201600155.

[13] Y.Y. Lai, X. Li, Y. Zhu, Polymeric active materials for redox flow battery application, ACS Appl. Polym. Mater. 2 (2020) 113–128, https://doi.org/10.1021/acsapm.9b00864.

[14] X. Wang, J. Chai, J. Jiang, Redox flow batteries based on insoluble redox-active materials. A review, Nano Mater. Sci. 3 (2021) 17–24, https://doi.org/10.1016/j.nanoms.2020.06.003.

[15] J. Winsberg, T. Hagemann, T. Janoschka, M.D. Hager, U.S. Schubert, Redox-flow batteries: from metals to organic redox-active materials, Angew. Chem. Int. Ed. 55 (2016) 2–28, https://doi.org/10.1002/anie.201604925.

[16] R. Chen, Redox flow batteries for energy storage: recent advances in using organic active materials, Curr. Opin. Electrochem. 21 (2020) 40–45, https://doi.org/10.1016/j.coelec.2020.01.003.

[17] S. Gentil, D. Reynard, H.H. Girault, Aqueous organic and redox-mediated redox flow batteries: a review, Curr. Opin. Electrochem. 21 (2020) 7–13, https://doi.org/10.1016/j.coelec.2019.12.006.

[18] V. Singh, S. Kim, J. Kang, H.R. Byon, Aqueous organic redox flow batteries, Nano Res. 12 (2019) 1988–2001, https://doi.org/10.1007/s12274-019-2355-2.

[19] Y. Liu, Q. Chen, P. Sun, Y. Li, Z. Yang, T. Xu, Organic electrolytes for aqueous organic flow batteries, Mater. Today Energy 20 (2021) 100634, https://doi.org/10.1016/j.mtener.2020.100634.

[20] F.R. Brushett, M.J. Aziz, K.E. Rodby, On lifetime and cost of redox-active organics for aqueous flow batteries, ACS Energy Lett. 5 (2020) 879–884, https://doi.org/10.1021/acsenergylett.0c00140.

[21] D.G. Kwabi, Y. Ji, M.J. Aziz, Electrolyte lifetime in aqueous organic redox flow batteries: a critical review, Chem. Rev. 120 (2020) 6467–6489, https://doi.org/10.1021/acs.chemrev.9b00599.

[22] E.W. Zhao, E. Jónsson, R.B. Jethwa, D. Hey, D. Lyu, A. Brookfield, P.A.A. Klusener, D. Collison, C.P. Grey, Coupled in situ NMR and EPR studies reveal the electron transfer rate and electrolyte decomposition in redox flow batteries, J. Am. Chem. Soc. 143 (2021) 1885–1895, https://doi.org/10.1021/jacs.0c10650.

[23] P. Navalpotro, J. Palma, M. Anderson, R. Marcilla, A membrane-free redox flow battery with two immiscible redox electrolytes, Angew. Chem. Int. Ed 56 (2017) 12460–12465, https://doi.org/10.1002/anie.201704318.

[24] P. Navalpotro, N. Sierra, C. Trujillo, I. Montes, J. Palma, R. Marcilla, Exploring the versatility of membrane-free battery concept using different combinations of immiscible redox electrolytes, ACS Appl. Mater. Interfaces 10 (2018) 41246–41256, https://doi.org/10.1021/acsami.8b11581.

[25] K. Gong, F. Xu, M.G. Lehrich, X. Ma, S. Gu, Y. Yan, Exploiting immiscible aqueous-nonaqueous electrolyte interface toward a membraneless redox-flow battery concept, J. Electrochem. Soc. 164 (2017) A2590–A2593, https://doi.org/10.1149/2.1241712jes.

[26] A.F. Molina-Osorio, A. Gamero-Quijano, P. Peljo, M.D. Scanlon, Membraneless energy conversion and storage using immiscible electrolyte solutions, Curr. Opin. Electrochem. 21 (2020) 100–108, https://doi.org/10.1016/j.coelec.2020.01.013.

[27] M.O. Bamgbopa, Y. Shao-Horn, R. Hashaikeh, S. Almheiri, Cyclable membraneless redox flow batteries based on immiscible liquid electrolytes: demonstration with all-iron redox chemistry, Electrochim. Acta 267 (2018) 41–50, https://doi.org/10.1016/j.electacta.2018.02.063.

[28] X. Li, Z. Qin, Y. Deng, Z. Wu, W. Hu, Development and challenges of biphasic membrane-less redox batteries, Adv. Sci. 2105468 (2022), 2105468, https://doi.org/10.1002/advs.202105468.

[29] S. Hou, L. Chen, X. Fan, X. Fan, X. Ji, B. Wang, C. Cui, J. Chen, C. Yang, W. Wang, C. Li, C. Wang, High-energy and low-cost membrane-free chlorine flow battery, Nat. Commun. 13 (2022) 1–8, https://doi.org/10.1038/s41467-022-28880-x.

[30] X. Wang, J. Chai, J. "Jimmy" Jiang, Redox flow batteries based on insoluble redox-active materials. A review, Nano Mater. Sci 3 (2021) 17–24, https://doi.org/10.1016/j.nanoms.2020.06.003.

[31] X. Wang, A. Lashgari, J. Chai, J. "Jimmy" Jiang, A membrane-free, aqueous/nonaqueous hybrid redox flow battery, Energy Storage Mater. 45 (2022) 1100–1108, https://doi.org/10.1016/j.ensm.2021.11.008.

[32] P. Navalpotro, C.M.S.S. Neves, J. Palma, M.G. Freire, J.A.P. Coutinho, R. Marcilla, Pioneering use of ionic liquid-based aqueous biphasic systems as membrane-free batteries, Adv. Sci. 5 (2018) 1–10, https://doi.org/10.1002/advs.201800576.

[33] P. Navalpotro, C. Trujillo, I. Montes, C.M.S.S. Neves, J. Palma, M.G. Freire, J.A.P. Coutinho, R. Marcilla, Critical aspects of membrane-free aqueous battery based on two immiscible neutral electrolytes, Energy Storage Mater. 26 (2020) 400–407, https://doi.org/10.1016/j.ensm.2019.11.011.

[34] B. Hu, C. Debruler, Z. Rhodes, T.L. Liu, Long-Cycling aqueous organic Redox flow battery (AORFB) toward sustainable and safe energy storage, J. Am. Chem. Soc. 139 (2017) 1207–1214, https://doi.org/10.1021/jacs.6b10984.

[35] E.S. Beh, D. De Porcellinis, R.L. Gracia, K.T. Xia, R.G. Gordon, M.J. Aziz, A neutral pH aqueous organic–organometallic redox flow battery with extremely high capacity retention, ACS Energy Lett. 2 (2017) 639–644, https://doi.org/10.1021/acsenergylett.7b00019.

[36] C. DeBruler, B. Hu, J. Moss, X. Liu, J. Luo, Y. Sun, T.L. Liu, Designer Two-Electron Storage Viologen Anolyte Materials for Neutral Aqueous Organic Redox Flow Batteries, Chem 3 (2017) 961–978, https://doi.org/10.1016/j.chempr.2017.11.001.

[37] B. Hu, C. Seefeldt, C. Debruler, T.L. Liu, Boosting the energy efficiency and power performance of neutral aqueous organic redox flow batteries, J. Mater. Chem. A 5 (2017) 22137–22145, https://doi.org/10.1039/c7ta06573f.

[38] A. Korshunov, A. Gibalova, M. Grünebaum, B.J. Ravoo, M. Winter, I. Cekic-Laskovic, Host-guest interactions enhance the performance of viologen electrolytes for aqueous organic redox flow batteries, Batter. Supercaps 4 (2021) 923–928, https://doi.org/10.1002/batt.202100018.

[39] Y. Liu, Y. Li, P. Zuo, Q. Chen, G. Tang, P. Sun, Z. Yang, T. Xu, Screening viologen derivatives for neutral aqueous organic redox flow batteries, ChemSusChem 13 (2020) 2245–2249, https://doi.org/10.1002/cssc.202000381.

[40] J. Huang, Z. Yang, V. Murugesan, E. Walter, A. Hollas, B. Pan, R.S. Assary, I.A. Shkrob, X. Wei, Z. Zhang, Spatially constrained organic diquat anolyte for stable aqueous flow batteries, ACS Energy Lett. 3 (2018) 2533–2538, https://doi.org/10.1021/acsenergylett.8b01550.

[41] B. Hu, C. DeBruler, Z. Rhodes, T.L. Liu, Long-Cycling Aqueous Organic Redox Flow Battery (AORFB) toward sustainable and safe energy storage, J. Am. Chem. Soc. 139 (2017) 1207–1214, https://doi.org/10.1021/jacs.6b10984.

[42] I. Montes, R. Marcilla, J. Palma, E. Ventosa, M. Vera, M. Sánchez Sanz, S.E. Ibañez, Redox flow Battery with immiscible electrolyte and flow through electrode, WO2021209585A1, 2020.

[43] J.C. Merchuk, B.A. Andrews, J.A. Asenjo, Aqueous two-phase systems for protein separation: studies on phase inversion, J. Chromatogr. B Biomed. Sci. Appl. 711 (1998) 285–293, https://doi.org/10.1016/S0378-4347(97)00594-X.

[44] H. Wang, S.Y. Sayed, E.J. Luber, B.C. Olsen, S.M. Shirurkar, S. Venkatakrishnan, U.M. Tefashe, A.K. Farquhar, E.S. Smotkin, R.L. McCreery, J.M. Buriak, Redox flow batteries: how to determine electrochemical kinetic parameters, ACS Nano 14 (2020) 2575–2584, https://doi.org/10.1021/acsnano.0c01281.

[45] R.S. Nicholson, Theory and application of cyclic voltammetry for measurement of electrode reaction kinetics, Anal. Chem. 37 (1965) 1351–1355, https://doi.org/10.1021/ac60230a016.